On the role of aortic valve architecture for physiological hemodynamics and valve replacement, Part I: Flow configuration and vortex dynamics

Pascal Corso *, Dominik Obrist

ARTORG Center for Biomedical Engineering Research, University of Bern, Bern, Switzerland

ARTICLE INFO

ABSTRACT

Aortic valve replacement has become an increasing concern due to the rising prevalence of aortic stenosis in an ageing population. Existing replacement options have limitations, necessitating the development of improved prosthetic aortic valves. In this study, flow characteristics during systole in a stenotic aortic valve case are compared with those downstream of two newly designed surgical bioprosthetic aortic valves (BioAVs). To do so, advanced three-dimensional fluid–structure interaction simulations are conducted and dedicated analysis methods to investigate jet flow configuration and vortex dynamics are developed. Our findings reveal that the stenotic case maintains a high jet flow eccentricity due to a fixed orifice geometry, resulting in flow separation and increased vortex stretching and tilting in the commissural low-flow regions. One BioAV design introduces non-axisymmetric leaflet motion, which reduces the maximum jet velocity and forms more vortical structures. The other BioAV design produces a fixed symmetric triangular jet shape due to non-moving leaflets and exhibits favourable vorticity attenuation, revealed by negative temporally and spatially averaged projected vortex stretching values, and significantly reduced drag. Therefore, this study highlights the benefits of custom-designed aortic valves in the context of their replacement through comprehensive and novel flow analyses. The results emphasise the importance of analysing jet flow, vortical structures, momentum balance and vorticity transport for thoroughly evaluating aortic valve performance.

1. Introduction

Aortic stenosis (AS) concerns the progressive deterioration and re-modelling of the leaflet tissue, which reduces its dynamics. This leads to an increased resistance for the blood to flow from the left ventricle to the aorta during systole and to the possibility for blood to flow back during diastole [1–3]. The long-term consequences of severe AS are very serious including heart failure and mortality is more than 90% within a few years after the onset of symptoms [4]. Valvular prostheses made from either rigid materials such as titanium or carbon, known as mechanical heart valves, or from biological tissue, known as bioprosthetic aortic valves (BioAV), have become a common solution for replacing the diseased aortic valve through a procedure called aortic valve replacement (AVR). AS prevalence increases with age and affects as many as 5% of the population after 75 years of age. AS is responsible for 300,000 surgical aortic valve replacements worldwide annually, a number that is expected to double by 2050 with the ageing population [5].

The performance of aortic valves surgically implanted and made from biological tissue such as porcine or bovine pericardium has been extensively investigated in the literature [1,3,6,7] but the link between valve design, flow features and leaflet motion has never been studied either experimentally or computationally. Bescek et al. [7] presented a computational characterisation of the turbulent features of the flow downstream of one bioprosthetic aortic valve model under peak systolic conditions. They showed that turbulence is a significant and detrimental factor for haemodynamic performance. However, Becsek et al. [7] did not analyse the downstream evolution of vortices from the specific aortic valve bioprosthesis under consideration. They also did not establish a connection between valve design, leaflet motion, the observed vortical structures and the spatial–temporal variations in vorticity. Moreover, they did not quantify the drag forces associated with the presence of the mentioned bioprosthetic aortic valve. In another study, Johnson et al. [8] investigated the impact of heart valve tissue thickness on the presence, nature and extent of leaflet flutter. While assuming that the cyclic strain behaviour observed when the valve leaflet's free edge flutters over the valve's lifetime causes additional induced cyclic loading, which may contribute to non-uniform or accelerated leaflet fatigue and deterioration, their study demonstrated that a significant reduction in valve material thickness can lead to detrimental leaflet flutter. Relying upon an immersogeometric analysis

---

framework to simulate the fluid–structure interaction problem and on a flutter-quantification methodology, their results highlighted the impact that a single parameter can have on both the structural performance of the tissue and the blood flow behaviour throughout the whole cardiac cycle. Nevertheless, flow quantities related to turbulence were not calculated and the conclusions as to the impact of the flutter motion on the flow was limited to the visualisation of iso-surfaces of instantaneous velocity and vorticity field close to the valve and in the curved ascending aorta model. Most recently, Morany et al. [9] conducted a computational study of the fluid–structure interaction problem arising in healthy tricuspid and biscuspid aortic valves (TAV and BAV). For this purpose, they strongly coupled, using a partitioned approach, the lattice Boltzmann method (LBM) to solve the blood motion equation to a Finite Element (FE) method to solve the elastic body motion equation. To model the constitutive relationship of the porcine leaflets, they considered a symmetric collagen fibre network (CFN) embedded in an elastin matrix for each valve leaflet. The distribution of these fibres was obtained by averaging the maps of fibre bundles observed under a microscope for 15 porcine leaflets [10]. Morany et al. concluded that their LBM-FE FSI approach was able to reliably assess velocity, and more specifically the velocity oscillations occurring at mid-diastole downstream of the TAV, and wall shear stress throughout the whole cardiac cycle in the vicinity of a TAV and a BAV. However, it is important to note that the comparison was limited to expected ranges of values and no detailed examination of spatial distributions for both velocity and wall shear stress fields was carried out. The resolution of the fluid lattices considered in Morany et al. only permitted the analysis of large-scale flow features, thus neglecting the small-scale velocity fluctuations that are of great importance when characterising the transition to turbulence in the aorta. With regard to the flow topology near healthy or calcified aortic valves, a series of studies (e.g., [11,12]) have described so-called Lagrangian coherent structures (LCS) in the vicinity of aortic valves, shedding light on dominant flow features such as recirculation regions, vortex boundaries or separation profiles and uncovering kinematic processes organising fluid mixing. The LCS are ridge boundaries or material lines obtained by computing Finite-Time Lyapunov Exponents (FTLE) from the integration of massless particle trajectories into blood flow. Stable and unstable manifolds are obtained by computing the forward or backward integration FTLE, with high values corresponding to repelling or attracting LCS, respectively. As stated by Shadden et al. [12], LCS offers a method to unambiguously delineate the aortic jet region from the surrounding low-velocity region and hence more precisely compute the area of the jet compared to approximated clinical approaches. In Olcay et al. [11], the analysis of stable manifolds indicated the presence of a region filled with stagnant fluid that was thicker upstream of calcified leaflets and a recirculation region in the sinus shifted towards the leaflet tip due to calcification, potentially preventing an appropriate closure of the leaflets. While the computation of LCS represents an interesting approach for distinguishing regions in blood flow characterised by strong hyperbolicity in particle dynamics, allowing for the foregrounding of topological markers, this approach has fallen short in characterising the complexity of three-dimensional aortic flows due to computational expenses and the difficulty in making sense of the intricacy of LCS as a consequence of turbulence throughout the cardiac cycle. Moreover, the works in [11,12] utilising LCS computation and analysis assumed simplified geometries for the aortic valves as well as approximated linear elastic constitutive laws for the leaflet material properties. In addition, the correlation between LCS, valve architecture and leaflet motions was not investigated.

The present work is the first part of a comprehensive two-part study. The analysis of blood motion focuses on characterising the flow organisation by describing the distribution of velocity magnitude and the dynamics of coherent vortical structures downstream of three different valvular configurations. The temporal evolution of the terms of the vorticity dynamics equation is also investigated. Besides, two

novel quantities corresponding to the vortex advection and stretching terms, projected onto the eigenbasis of the vorticity gradient and rate-of-strain matrices, respectively, are introduced. To the best of our knowledge, a comprehensive computational study and detailed analysis encompassing various designs of aortic valve bioprostheses along with a comparative analysis to a severe stenotic case have not been previously undertaken. This work contributes to the advancement of optimally designed and patient-customised aortic valves. Through dedicated flow analysis, it comprehensively investigates *in silico* the flow configuration near a pathological aortic stenosis, comparing it to the flow characteristics downstream of two surgical valve bioprostheses and of native aortic valves whose performance was assessed *in vivo* using four-dimensional phase-contrast magnetic resonance imaging, as presented in a work from literature [13]. The two valve bioprostheses investigated *in silico* in the present two-part study have undergone modifications in their leaflet geometry by thoughtfully changing selected geometric parameters. The connection between the two BioAV valve designs, the subsequent leaflet motion and the encountered aortic flow features is revealed. The second part of the study explores the flow-energy-based mechanisms downstream of the two BioAVs in comparison to those observed downstream of a severe aortic stenosis. It also establishes a correlation between spatial maps of kinetic energy carried by the leaflets of the two BioAVs and spatial maps of kinetic energy calculated within the flow over spherical regions.

2. Methods

2.1. Geometrical models and leaflet geometry parametrisation

As far as the severely calcified aortic valve case is concerned, the geometry of the curved aorta was obtained from high-resolution magnetic resonance imaging (MRI) scan (cf. Fig. 1 (a, b)) and has a diameter at the sino-tubular junction (STJ) d_{STJ}^{sten} of 25 mm (see Fig. 1 (e)). A patient-based geometry of stenosis was added to the sino-tubular extremity. The eccentric stenotic orifice subsequent to the calcification of a tricuspid aortic valve is shown in Fig. 1 (e, f). The reduction in cross-sectional area through the orifice is about 80% [1,2,14]. Within the scope of this study, only the straight section of the ascending aorta is considered when comparing the jet flow structures present in the vicinity of the orifice for the stenotic and bioprosthetic cases (see Fig. 1 (b, c)). Concerning the bioprosthetic valve cases, the geometry of the aortic root (AR) including the sinus of Valsalva (SOV) geometry is similar to the one presented in Bescek et al. [7]. The main dimensions of the sinus portion and the straight aorta are shown in Fig. 1 (g, h). The geometry of the bioprosthetic heart valves, including three leaflets and a supporting ring, corresponds to an approximate reproduction of the commercial valve *Edwards Intuity Elite 21 mm* (Edwards Lifescience, Irvine, CA, USA). The leaflets are made from glutaraldehyde-fixed bovine pericardium and are mounted on a rigid ring made of polymer supported by a nitinol wireframe and covered with fabric. The BioAV models are introduced in the AR, as shown in Fig. 1 (d).

To test the influence of different leaflet geometries of BioAV on their kinematics and on the flow characteristics at peak systole, two new geometrical configurations (with reference VLth30 and Ulth0) for the 500-micron-thick leaflets have been designed (cf. Fig. 2 (b, c)). Besides, it is assumed that the designed initial leaflet position corresponds to the stress-free configuration. As shown in Fig. 2 (b) and (c), the two geometries of the newly designed leaflets vary with each other based on three features of the leaflet [15]: (i) the belly curve, i.e. the curve obtained by longitudinally cutting the leaflet in half (cf. Fig. 2 (b, c, e)) ; (ii) the free edge, i.e. the leaflet extremity not attached to the ring (Fig. 2 (a)); (iii) the scallop or attachment curve, i.e. the leaflet extremity attached to the ring (Fig. 2 (d)). Each feature of the designed leaflets is defined based on different parameters that are summarised in Fig. 2 (f). The belly curve with centred and normalised coordinates is defined by two parameters *a* and *b* of the hyperbolic sine function
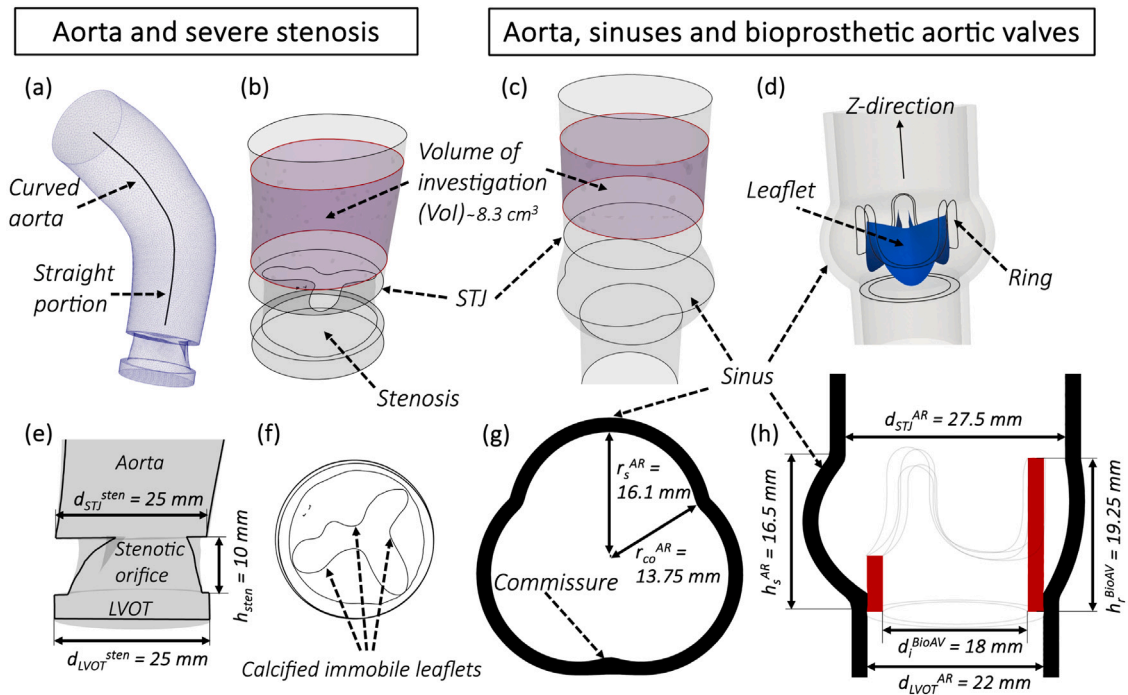
Fig. 1. Geometrical description of ascending aorta models (a, b, c) including an aortic stenosis model due to calcified leaflets (b, e, f) as well as two bioprosthetic aortic valves inserted (d) in a realistic aortic root geometry (c, d, g, h).

as shown in Fig. 2 (e). Depending on the geometry of the ring and on the other two features, the belly curve is dimensionalised leading to two radial lengths (ΔX_{Ulth0}, ΔX_{VLth30}), two axial lengths (Δh_{Ulth0}, Δh_{VLth30}) and two belly curve lengths ($l = 13$ mm and $L = 14.5$ mm). The values of belly curve length for both valve leaflet designs are in line with the range of mean values for the so-called geometric height measured via cardiac computed tomography in 123 adults by Izawa et al. [16]. The free edge is characterised by the angle θ between the plane perpendicular to the centreline of the straight aorta passing through the intersecting points of the free edge and scallop curve and the plane defined by the centre point of the free edge and the intersecting points of the free edge and scallop curve. The coaptation length feature reported by Izawa et al. [16] is directly related to the free edge angle feature. The two proposed free edge angle values in the present study cover the range of coaptation length values provided in [16] for 123 adult participants. The shape of the scallop curve of the leaflets to the valve ring is classified as V- or U-shaped depending on its resemblance to the corresponding letter.

The following nomenclature consisting of a sequence of letters and digits is used to refer to the two leaflet geometries: attachment curve shape - length of the belly curve - th - value of θ in arcdegree (cf. Fig. 2 (b, c, f)).

2.2. Numerical setups

The direct numerical simulation (DNS) of blood flow in the stenosed aorta was conducted with the open-source code NEK5000 [17]. This code is based on a spectral element method [18] solving the Navier–Stokes equations for Newtonian and incompressible flows. Details on the numerical methods used and on the implementation of the direct numerical simulation can be found in Corso et al. [2]. The wall of the stenosed aorta is treated as rigid in the DNS for this case. Indeed, since peak systolic conditions are simulated, it is assumed that the stenotic orifice aperture (see Fig. 1 (f)) does not vary over time as a consequence of the extensively calcified leaflets. Furthermore, as noted by Corso et al. [2], the smallest resolved scale in the direct numerical simulation of the aortic stenosis case is approximately 25 μm. The Kolmogorov

length scale in the ascending aorta varies between 20 and 75 μm, depending on the specific regions considered in the aorta [2,19]. It is worth noting that the Reynolds number Re_o calculated at the stenotic orifice averages at 3,800 over systole. Re_o is determined by considering the diameter of the circular area corresponding to the stenotic orifice area and the spatially averaged velocity at the orifice. The Dirichlet inflow boundary conditions on the three components of velocity over the inflow cross-section upstream of the stenosis are prescribed such that pseudo-steady systolic conditions (taking into account flow variations measured during *in vitro* experiments) are simulated reaching a mean systolic flow rate of 12 L/min [2,14] (cf. Fig. S11 in the SI). With respect to the simulation of the bioprosthetic aortic valve cases, the computational method for the high-fidelity simulation of the blood flow and the mechanics of the leaflets relies on a fluid–structure interaction (FSI) approach based on a modified immersed boundary method taking into account a deformable structure (i.e. the valve and the aorta) embedded into a fixed fluid domain [20,21]. The Navier–Stokes equations for incompressible flows of Newtonian fluid are solved on a Cartesian grid (of dimension $40 \times 40 \times 80$ [mm³] with $120 \times 120 \times 288$ points for each direction) using sixth-order compact finite differences on staggered grids for each velocity components and pressure [22]. Moreover, an explicit low-storage third-order accurate Runge–Kutta time stepping scheme for the advective term and a semi-implicit Crank–Nicolson scheme for the temporal discretisation of the diffusive term [23] are used. Additional information regarding the solving algorithms employed to solve the large system of equations for the fluid sub-problem can be found in [22,23]. Grid stretching is implemented to ensure that the grid point distance near the BioAV orifice is 40 μm, while it increases to approximately 100 μm near the jet shear layers further downstream. As detailed in the second part of the current study [19], the Kolmogorov length scale near the valve orifice ranges between 40 and 80 μm. With these grid parameters, all scales of the flow are then adequately resolved, enabling the direct numerical simulation of transitional blood flow in the straight ascending aorta for the two BioAV cases considered in this study. The elastodynamics equation is solved on a moving tetrahedral mesh (i.e. on a Lagrangian frame of reference) of about 200,000 affine elements using the finite-element formulation and a second-order accurate semi-implicit central
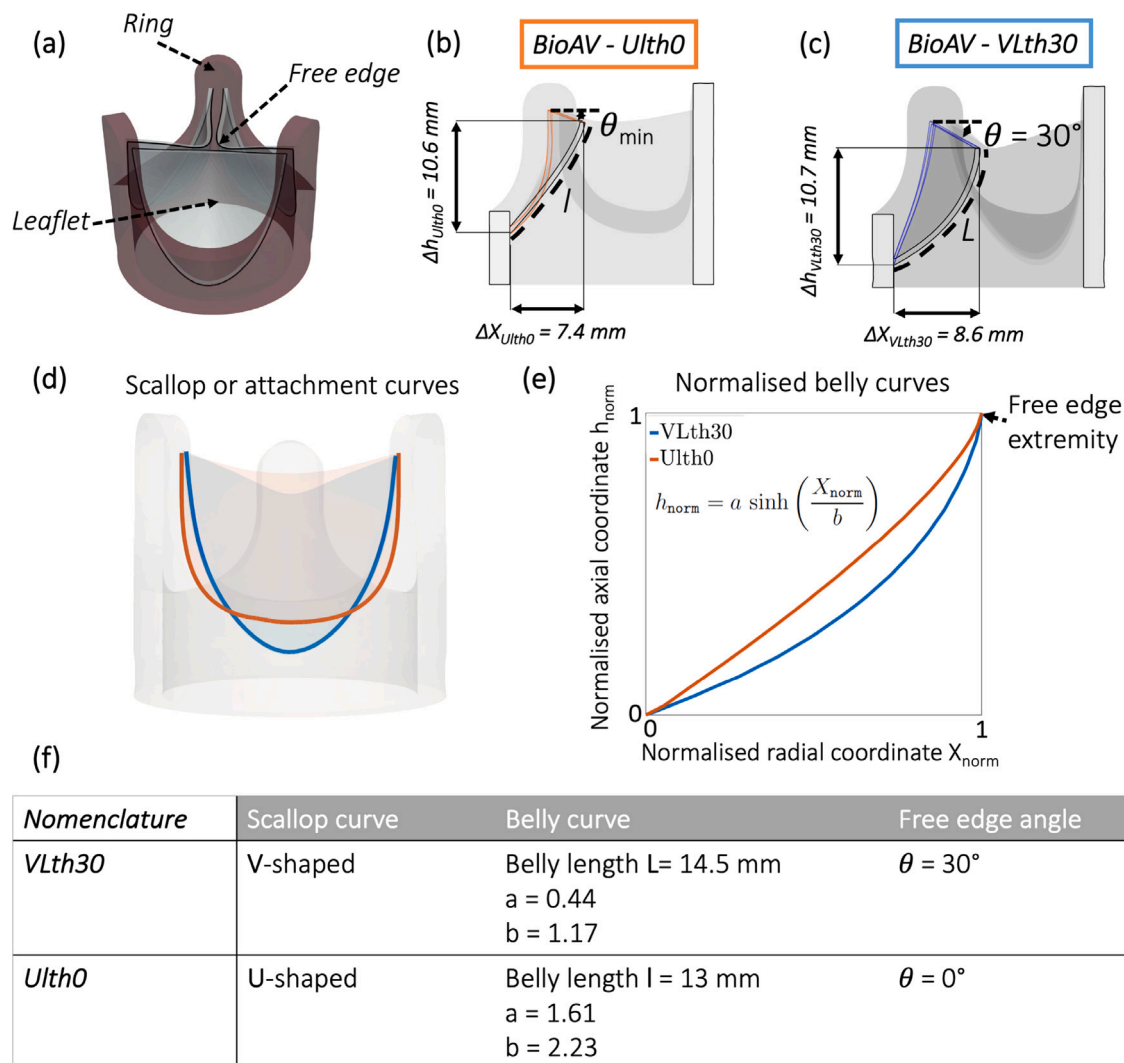
Fig. 2. Geometrical description of the two different geometries of valve bioprostheses (a, b, c) obtained by modifying the leaflet shape (d, e), the valve ring being the same for both valves (a). The parameters describing the three features, i.e. the belly curve, the free edge and the shape of the attachment curve, for the leaflet geometry generation, are summarised in (f).

difference time-stepping scheme [21,22,24]. All the structural parts (i.e. aorta, leaflets and ring) share element nodes at their intersection. The Newton method is used to linearise the system of non-linear equations for the solid sub-problem and the linear system of equations is solved using a generalised minimal residual iterative method (GMRES) with an additive Schwarz preconditioner [24,25]. The relative and absolute tolerance value on the residuals to stop the iterations for the resolution of the linear and non-linear systems is set to 10^{-6} and 10^{-8}, respectively [7]. The strong coupling of the Navier–Stokes and elastodynamics equations is based on a parallel variational transfer [26] of velocities (from fluid grid to solid mesh) and of reaction forces (from solid mesh to fluid grid) between non-matching discretisation points and elements' nodes. The fluid and solid sub-problems are solved synchronously with a time-step of 5×10^{-6} s. The formulation of the variational transfer corresponds to the equalities of the L^2-projections of velocity or forces between two non-overlapping meshes by defining a suitable space of Lagrange multipliers. The transfer operator is then assembled from mortar matrices computed by numerically integrating the Lagrange basis functions of the three spaces. A linear system is ultimately solved to obtain the projected velocities imposed as Dirichlet boundary condition at the fluid–structure interface of the solid sub-problem and the projected force density added as a source term to the blood flow momentum equation. An iterative procedure, stopped when

a prescribed relative tolerance of 10^{-6} is reached, is implemented to ensure velocity and force continuity at the fluid–structure interface [21, 26]. Concerning the material properties for the structural elements of the investigated FSI problems, a fibre-based model is used to characterise the nearly incompressible anisotropic material properties of the glutaraldehyde-pretreated bovine pericardium leaflets [21,22,27,28]. The six parameters of this constitutive model, including two families of fibres oriented at a fitted angle of 60° to each other, were regressed to match experimental bi-axial tensile test data [27]. The material properties of the aortic wall and the supporting ring of the leaflets are described by a linear elastic constitutive relationship (density: 1500 kg/m^3 (ring); 1100 kg/m^3 (leaflets, aortic root and aorta), bulk modulus: 3 MPa and shear modulus: 0.3 MPa) [7]. Following a well-established assumption [29], blood is modelled as a Newtonian fluid with a constant kinematic viscosity ν of 3.77×10^{-6} m$^2/s$, equal to the blood viscosity in the ascending aorta at the largest shear rate and a density ρ_f of 1060 kg/m^3.

Systolic flow conditions are considered in the computational study. A pressure drop across the valves and in the ascending aorta of 8 mmHg is imposed over a time span of 0.3 s [22]. In order to prescribe a pressure difference within a cylindrical region upstream of the valve [22], which corresponds to the left ventricle outflow tract (LVOT), a forcing term is introduced on the right-hand side of the

fluid momentum equation. This method is adapted from the concept of fringe regions or sponge layers as described in [30,31]. Periodic boundary conditions are imposed at the borders of the fluid Cartesian grid in which the structures are embedded. Therefore, the addition of fringe forcing terms in cylindrical regions allows for the imposition of flow conditions within the domain. This prevents the occurrence of an ill-posed problem since special spatial discretisation is required in the vicinity of the boundaries (for Dirichlet-, Neumann-, or Robin-type boundary conditions), especially for high-order finite differences [23]. Consequently, the inflow velocity undergoes gradual acceleration due to the pressure difference imposed by means of the additional forcing term given by the following equation:

$$\mathbf{f}_{inflow} = \begin{bmatrix} \frac{\lambda(l)}{\lambda_{max}} \frac{\Delta p_{inflow}}{h_{cyl}} \frac{1}{\rho_f U_{ref}^2} \\ \lambda(l) \left(0 - u_2/U_{ref} \right) \\ \lambda(l) \left(0 - u_3/U_{ref} \right) \end{bmatrix} [-], \tag{1}$$

where $\lambda(l)$ is a damping function vanishing in the physical domain, flat in most of the interior of the cylindrical fringe region, while decaying smoothly to 0 at the boundaries of the fringe region [31]. λ_{max} is the magnitude of the damping function. Δp_{inflow} is equal to 16 mmHg (= 2133.2 Pa). U_{ref} is the reference velocity used to non-dimensionalise the velocity vector $\mathbf{u}$ in the Navier–Stokes equations. h_{cyl} is the length of the cylindrical fringe region. A coordinate system projection is performed such that the pressure difference imposed by $\mathbf{f}_{inflow}$ along direction l aligns with the normal to the inflow cross-section and in the streamwise direction. u_2 and u_3 are then the velocity components perpendicular to the axis of the cylindrical fringe region. These components in the fringe region are forced to be equal to 0. In addition, a second cylindrical fringe region is positioned at the outflow extremity of the aorta model. Its purpose is twofold: firstly, to emulate the resistance (by applying a resistive pressure) arising from the curved portion of the aorta (which is not modelled in the pericardial bioprosthesis cases) and secondly, to attenuate the flow fluctuations that might otherwise flow back due to the periodic boundary conditions prescribed on the fluid Cartesian grid [22]. The expression governing the forcing term in the second cylindrical fringe region shares a similar form with Eq. (1), except that $\Delta p_{outflow}$ is set to −8 mmHg (= −1066.6 Pa). A third cylindrical fringe region cancelling out the radial velocity components with a reduced width and placed before the inflow fringe region is finally added from time instant 0.1s onward (after reaching a peak flow rate of about 16 L/min [1]) to model the gradual flow deceleration occurring from time instances 0.1s to 0.3s (see Fig. S11 in the SI). Similarly to the simulation setup for the aortic stenosis case, the reference Reynolds number at the valvular orifice Re_o is equal to 3,800 in the BioAV cases. This Re_o corresponds to the Reynolds number computed by taking the average velocity at the valvular orifice and the diameter of the circular area corresponding to the BioAV orifice area over the acceleration and deceleration phases occurring throughout systole (see Fig. S11 in the supporting information (SI)). These phases result from the use of the three fringe regions.

2.3. Vortex structures, dynamics and stretching

The instantaneous vorticity transport equation, derived by taking the curl of the three-dimensional momentum Navier–Stokes equation and using vector identities, is expressed as follows:

$$\frac{D\boldsymbol{\omega}}{Dt} = \underbrace{\frac{\partial \boldsymbol{\omega}}{\partial t}}_{L_{\boldsymbol{\omega}}} + \underbrace{\mathbf{u} \cdot \nabla \boldsymbol{\omega}}_{A_{\boldsymbol{\omega}}} = \underbrace{\boldsymbol{\omega} \cdot \mathbf{L}}_{S_{\boldsymbol{\omega}}} + \underbrace{\nu \nabla^2 \boldsymbol{\omega}}_{D_{\boldsymbol{\omega}}}. \tag{2}$$

with $\mathbf{u}$, the velocity vector; $\boldsymbol{\omega} = \nabla \times \mathbf{u}$, the vorticity vector; $L_{\boldsymbol{\omega}}$, the local vorticity acceleration; $A_{\boldsymbol{\omega}}$, the vorticity advection tensor; $S_{\boldsymbol{\omega}}$, the vorticity straining tensor including vorticity stretching (diagonal entries of $S_{\boldsymbol{\omega}}$) and tilting (off-diagonal entries of $S_{\boldsymbol{\omega}}$); $D_{\boldsymbol{\omega}}$, the vorticity diffusion tensor. Of particular interest in this study is the vortex stretching term as the latter represents the rotational acceleration (or deceleration)

brought about due to rate-of-strain $\mathbf{L}$ parallel (or anti-parallel) to the vorticity vector $\boldsymbol{\omega}$. As shown in Eq. (2) for three-dimensional viscous flows, the rate of change of vorticity is dependent on the stretching, tilting and diffusion terms. A high and positive stretching term increases the rate of change of vorticity (phenomenon called amplification) and because of the conservation of the angular momentum, vortex filaments are confined as a consequence of the decrease in the coherent vortex radius [32]. Vortex tilting or turning represents the deflection of the vortex line or core caused by velocity gradients perpendicular to the direction of the vorticity vector. At moderate Reynolds numbers, the diffusion term is predominant in the smallest length scales of the flow except at the wall where viscous forces dominate. The magnitude of the vorticity advection $A_{\boldsymbol{\omega}}$ and straining terms $S_{\boldsymbol{\omega}}$ is investigated. Nonetheless, in order to take into account the orientation of the rate of strain $\mathbf{L}$ in the blood flow in relation to the vorticity vector, a projected vortex stretching $\Pi^{S_{\boldsymbol{\omega}}}$ is introduced and defined as the vorticity vector projected onto the eigenvectors of the rate-of-strain tensor $\mathbf{L} = 1/2 \left(\nabla \mathbf{u} + \nabla \mathbf{u}^T \right)$ and multiplied by the eigenvalues of this tensor:

$$\Pi^{S_{\boldsymbol{\omega}}} = \left(\boldsymbol{\omega} \cdot \mathcal{V}_{\mathbf{L}} \right) \cdot \lambda_{\mathbf{L}}, \tag{3}$$

with $\mathcal{V}_{\mathbf{L}}$, the eigenvectors of $\mathbf{L}$ and $\lambda_{\mathbf{L}}$, the eigenvalues of $\mathbf{L}$. A similar definition is used to calculate a projected vorticity advection $\Pi^{A_{\boldsymbol{\omega}}}$ by computing the eigenvectors and eigenvalues of the vorticity gradient.

2.4. Experimental validation of the numerical models

The validation of the direct numerical simulation results in the stenosed aorta is documented in Corso et al. [14], where they are compared to data from *in vitro* time-resolved three-dimensional flow MRI. The fields compared include velocity magnitude, Reynolds stresses and helicity. With respect to the experimental validation of the fluid–structure interaction computational model of the bioprosthetic aortic valve case from *in vitro* experiments, Fig. 3 shows the good agreement both qualitatively and quantitatively between the numerical FSI results and *in vitro* measurements [6,33]. The leaflet kinematics during valve opening for the VLth30 BioAV (see Fig. 3 (a)) closely matches that recorded at three time instants with a high-speed camera and presented in [6] (cf. Fig. 1 (b)). Furthermore, the comparison of the area at the vena contracta between the numerically and experimentally evaluated values over systole is presented in Fig. 3 (c). We notice a good agreement of the VLth30 curve obtained from the numerical flow velocity data with the diamond-shaped markers representing the area calculated based on the phase-averaged velocity field obtained from tomographic particle image velocimetry (tomo-PIV) measurements [33]. The discrepancies for the different time points over systole between the blue line representing the area downstream of the VLth30 BioAV case and the experimentally evaluated area downstream of the *Edwards Intuity Elite* BioAV (Edwards Lifesciences, Irvine, CA, United States) amounts to 6.7% of the experimental evaluation. The latter has a random uncertainty due to the finite number of samples for statistics acquisition on the area assessed from the tomo-PIV phase-averaged velocity data of 5% [33,35]. From the graph at Fig. 3 (c), we also observe that, for the VLth30 BioAV case, the area where the flow velocity is the highest periodically varies in time at variable frequencies between 18 and 30 Hz [36]. Conversely, the BioAV with Ulth0 design does not exhibit periodic motion of the three leaflets during peak systole (refer to Fig. S1 (a, c) in the SI), unlike the VLth30 case where the three leaflets move periodically at distinct frequencies [36] and asymmetrically relative to the centreline of the aortic root (see Fig. S1 (b, d) in the SI). Interestingly, the trend of the orifice area predicted over systole by Shadden et al. [12] using backward time FTLE fields for their simulated blood and aortic valve dynamics aligns with that of the Ulth0 BioAV case in the present study. However, owing to discrepancies in the modelled leaflet mechanics, the maximum jet area obtained in Shadden et al.'s work is 15% smaller (1.7 cm^2) than that obtained for the Ulth0 case (Fig. 3 (c)). Moreover, the flow characteristics highlighted by the
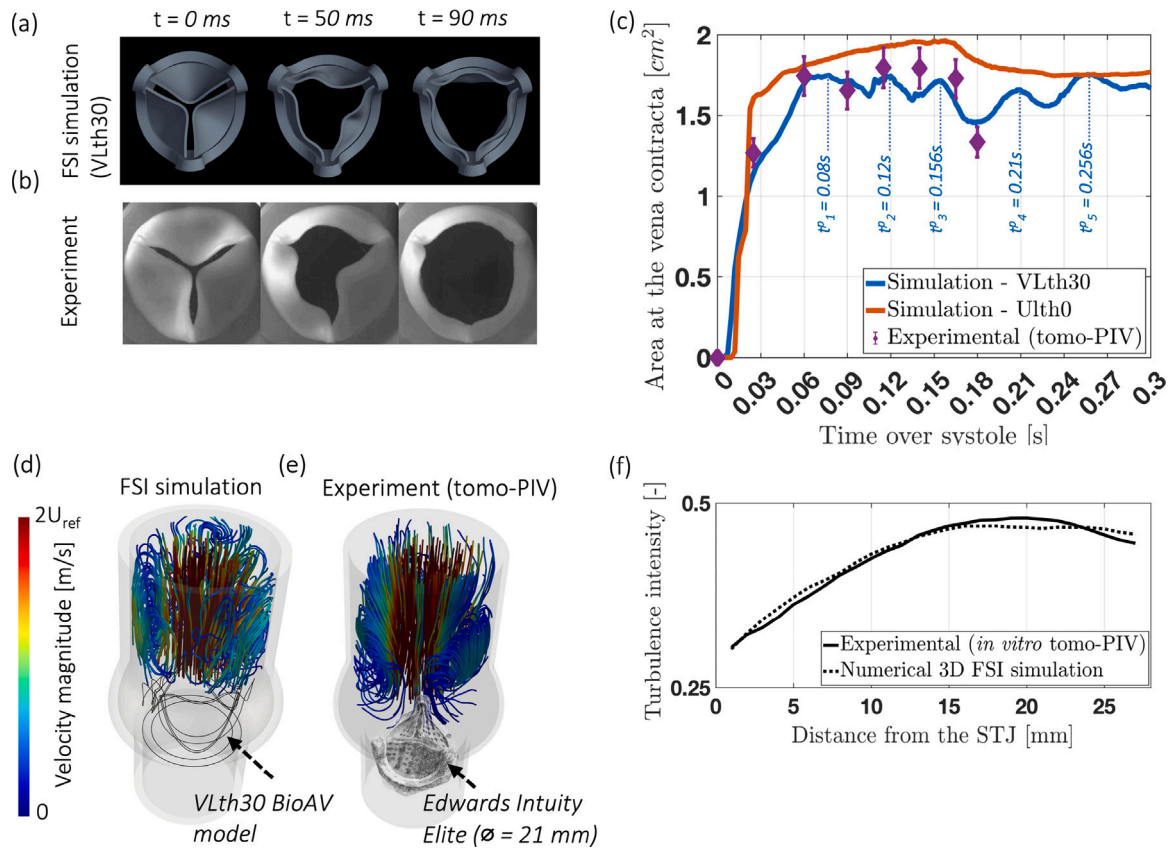
Fig. 3. Experimental validation of the FSI numerical model under peak systolic conditions. Leaflet opening (a) simulated for the VLth30 bioprosthetic valve case and (b) recorded by a high-speed camera during *in vitro* experiments [6] (c) Area at the vena contracta downstream of the two simulated BioAV cases obtained from the FSI numerical simulations and downstream of the *Edwards Intuity Elite* BioAV extracted from the flow field measured using the tomographic particle image velocimetry technique [33]. (d) Streamlines along the velocity field averaged over systole downstream of the VLth30 valve model. (e) Streamlines along the phase-averaged velocity obtained from tomo-PIV measurements. (f) Non-dimensional slice-averaged turbulence intensity from the simulation (VLth30 BioAV case) and from tomo-PIV experiments.

streamlines of the time-averaged velocity field obtained from the 3D FSI simulation are in line with those observed in experimental tomo-PIV data as depicted in Fig. 3 (d, e). The tomo-PIV data were acquired using a silicone phantom model of the ascending aorta with the *Edwards Intuity Elite* valve positioned in the sinus of Valsalva portion of the aorta model [33]. For comparison, the experimental velocity field was phase-averaged over peak systole. Notably, a high-velocity jet is present in the middle of the aorta, as indicated by streamlines aligned with the aorta's centreline. Additionally, recirculation zones are observed and align with the three posts of the BioAV ring. The curves in Fig. 3 (f) showing slice-averaged turbulence intensity, which represent the magnitude of velocity fluctuations owing to turbulence relative to the strength of the mean flow velocity, are nearly coincident for various slices perpendicular to the centreline of the ascending aorta. The discrepancy between the two curves averaged over the centreline amounts to 1.9% of the experimentally derived turbulence intensity. The random uncertainty in the turbulence intensity quantity derived from tomo-PIV phase-averaged velocity fields is estimated to be approximately 14%, with the uncertainty in turbulent kinetic energy estimated to be about 10%. This observation underscores the remarkable consistency between the *in vitro* experiment utilising the silicone phantom model and the numerical FSI simulation with the VLth30 BioAV design. A more in-depth analysis of the correlation between the kinetic energy carried by the leaflets and the kinetic energy calculated in the flow over spherical regions is presented in the second part of this study [19]. Fig. 6 presents the L1-norm of vorticity averaged over two downstream planes and over systole for different valvular configurations. We observe that the *in vitro* evaluation of vorticity downstream of the *Edwards Intuity Elite* BioAV, obtained from tomo-PIV data, is comparable to that of the

vorticity downstream of the VLth30 BioAV case calculated *in silico*. The difference between the two cases represents 7.2% of the taxicab norm of the vorticity downstream of the severely stenosed case. Through an uncertainty propagation calculation, where the independent variable is the phase-averaged velocity field, the random uncertainty for the vorticity computed *in vitro* amounts to approximately 9%.

3. Results and discussion

3.1. Jet flow configuration

Fig. 4 presents the velocity magnitude in a plane at a distance of 10 mm from the STJ (plane 1) as well as the evaluation of the eccentricity of the jet centre (white dots in Fig. 4) in relation to the centre of the circular cross-section (black dot in Fig. 4). The eccentricity distance, denoted as ε_c is defined as the distance between the black and white dots in Fig. 4. The eccentricity angle, represented by α_c, is the angle formed between these two dots, measured in relation to the horizontal direction starting from the black dot as a reference. Positive angles are counted in the counter-clockwise direction, while negative angles are measured in the clockwise direction. In the stenotic case, the eccentricity angle α_c of $-5°$ to $5°$ and eccentricity distance ε_c of about 2 mm do not significantly vary over time as the orifice geometry is immobile due to the severely calcified leaflets (see Fig. 1 (f)). Moreover, the regions situated between commissures 1–2 and 2–3 (cf. Fig. 4) exhibit elevated velocity magnitudes that extend from the jet, in contrast to the region between commissures 1–3. This trend is further highlighted in Fig. S6 of the supplementary information illustrating vortex straining magnitude in the proximal plane p1. In
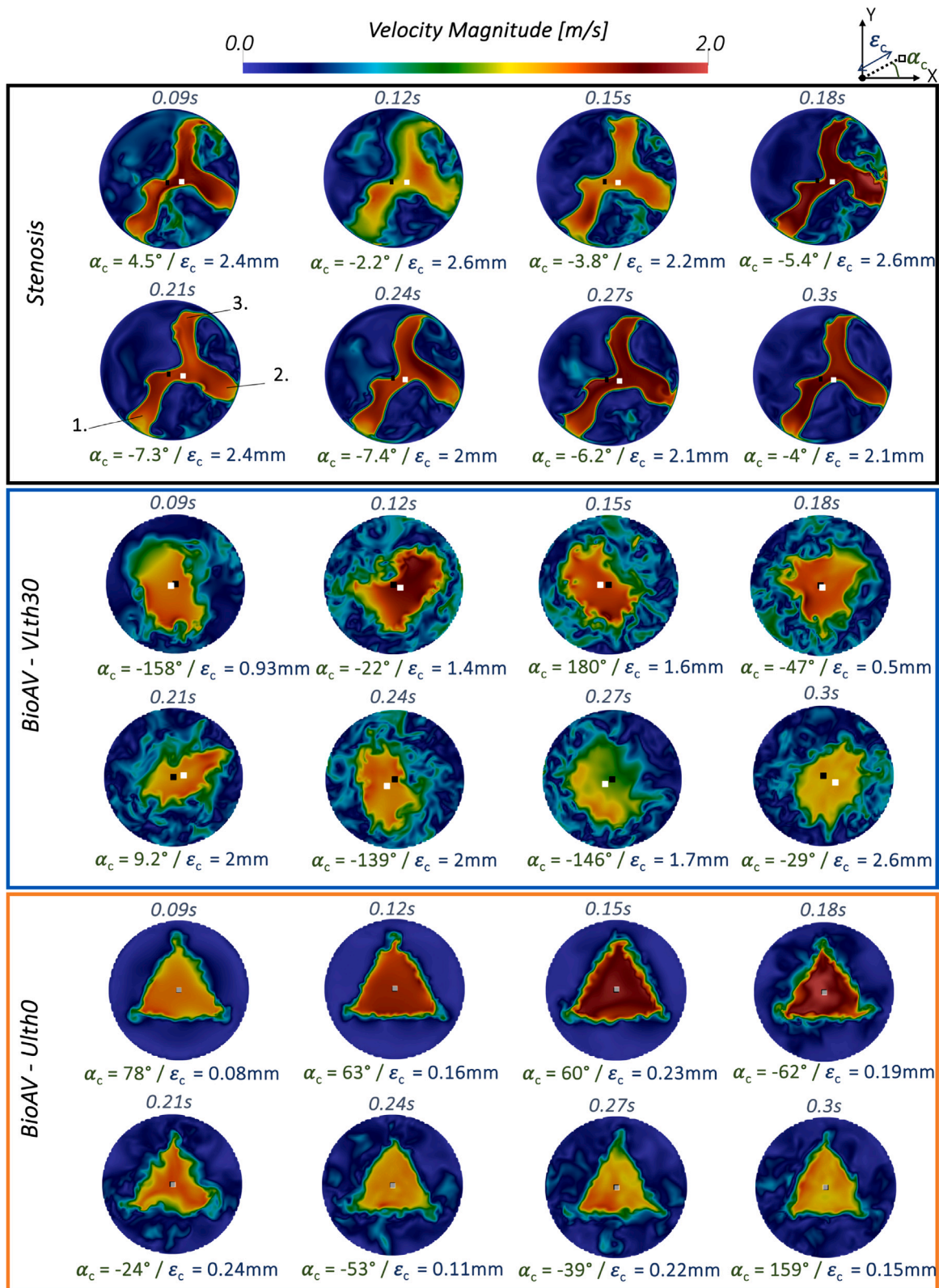
Fig. 4. Jet geometries (highlighted by velocity magnitude) for the three valvular cases at 8 time instances. The plane of investigation is positioned at a distance of 10 mm from the sino-tubular junction (STJ). The eccentricity from the centre of the circular cross-section is quantified by the distance ε_c and the azimuthal angle α_c in the plane. The centre of the cross-section is displayed by a black dot while the centre of mass of the jet region is represented by a white dot.

fact, we observe that elevated values of vortex straining magnitude are predominantly located between commissures 1–2 and 2–3. Conversely, within the area between commissures 1–3, the magnitude of vortex straining is negligible. At time instant $t = 0.12$ s, the velocity magnitude

in the trilobal jet drops, which is represented by a 30% decrease in the maximal velocity magnitude. The corresponding shear layers present smaller velocity gradients at this instant and are thicker. In Fig. S6, this trend is indicated by a decrease in the vortex straining magnitude.
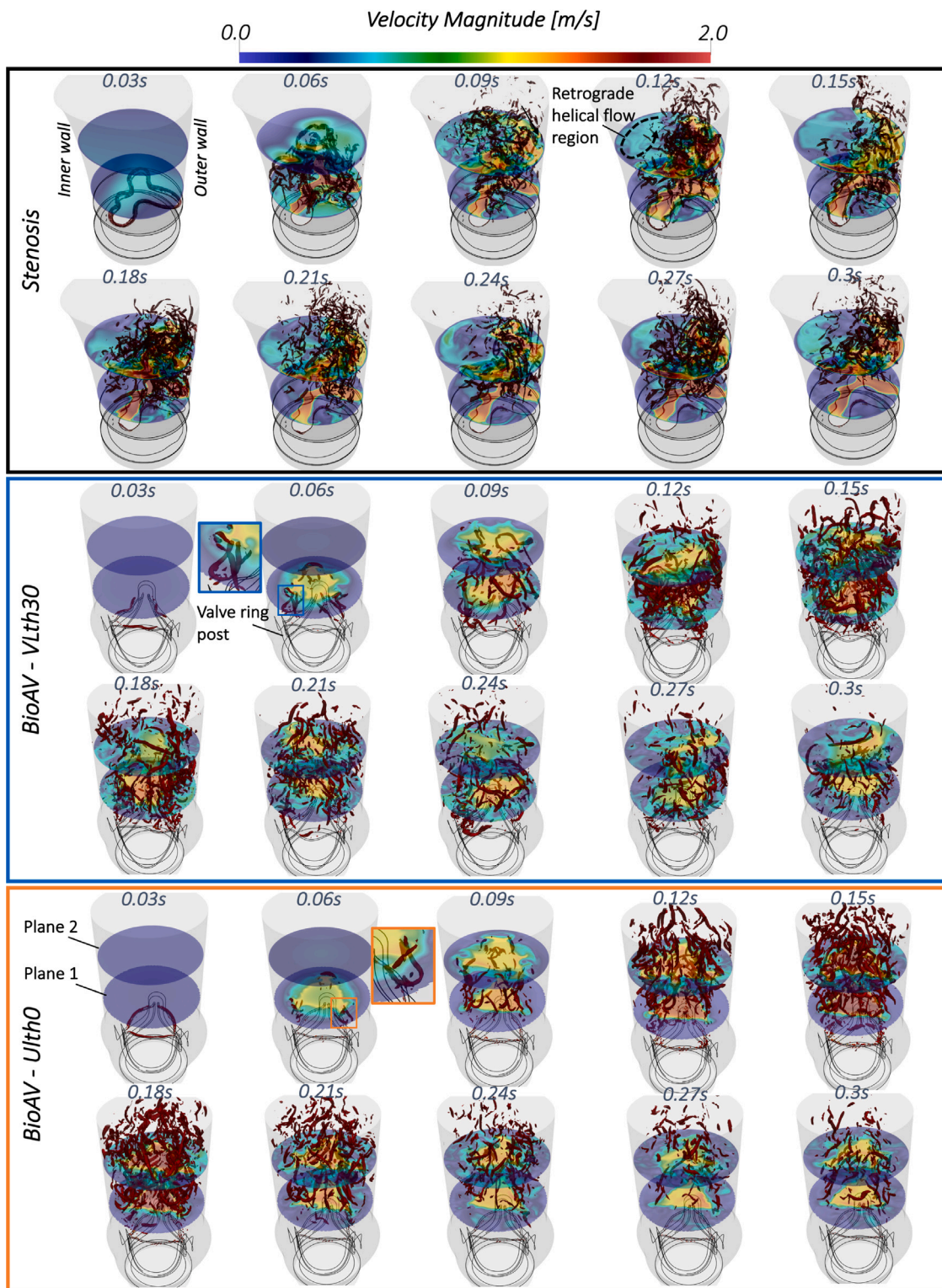
Fig. 5. Coherent vortical structures downstream of the considered severe aortic stenosis and of the two newly designed bioprosthetic aortic valves. The vortical structures are highlighted using a negative value for the λ_2 criterion proposed by Jeong and Hussain [34]. Velocity magnitude in two transverse planes (normal to the centreline) is also displayed. The time between two consecutive images is equal to 0.03s.

From 0.21s until 0.3s, the velocity magnitude in Fig. 4 indicates a more ordered separation between the main high velocity jet flow and the surrounding secondary low velocity flow. In Fig. S6 and Fig. 7 (a), this is revealed by a decrease in the values of $\|S_\omega\|$ over the proximal plane or averaged over the volume of investigation (VoI). Concerning the VLth30 BioAV case, the eccentricity distance and angle vary throughout

the systolic phase with higher eccentricity distances observed from $t = 0.21$ s onward. This is a direct consequence of the three leaflets moving asymmetrically with a displacement magnitude amplitude of 1.5 to 2 mm (see Fig. S1 in the supporting information (SI)). From Fig. S1, it is also noteworthy that the amplitude and difference in the three leaflets' position in relation to their initial position is more pronounced

from $t = 0.21$ s onward. Besides, as compared to the stenotic case, the motion of the leaflets and of the connected flow motion leads to a 10 to 20% smaller maximum velocity in the jet reaching peak values between $t = 0.12$ s and $t = 0.15$ s as shown in Fig. S3 (a). The velocity magnitude distribution in the region surrounding the jet is much less organised and presents larger velocity values as compared to the stenotic case due to the leaflet motion pushing blood in this region and promoting mixing of high and low velocity zones. With regard to the Ulth0 bioprosthesis case, given the almost immobile leaflets at peak systole (see Fig. 3 (c) and Fig. S1), the eccentricity distance ε_c is negligible. The shape of the jet is well defined and triangular. Between time instants $t = 0.15$ and $t = 0.21$ s, an instability is observed in the shear layer between the high-velocity jet (with a maximum velocity of 2 m/s, as shown in Fig. S3 (a)) and the surrounding quiescent region. This instability is characterised by the emergence of wavy irregularities in the velocity distribution at the borders of the triangular jet. It arises from the entrainment of high-velocity fluid elements into the region of lower velocity, subsequently pushing the low-velocity fluid towards the high-velocity flow region. This change in the velocity distribution and the creation of vortices along the shear layer interface is known as the Kelvin–Helmholtz instability (KHI) [37]. In the Ulth0 case, this instability, which breaks the flow axisymmetry, is likely to be accentuated by the flow deceleration that begins at $t = 0.1$ s and is imposed by the inflow conditions (see Fig. S11 in the SI). Finally, it is of relevance to mention that the fixed triangular-shaped jet described in the Ulth0 valvular case issuing from the valve leaflets has been also noted in Corso et al. [1] throughout systole and by means of three-dimensional particle tracking velocimetry measurements, downstream of a Medtronic (Minneapolis, Minnesota, USA) Evolut R transcatheter aortic valve. In the study by Corso et al. [1], another transcatheter valve, namely the CoreValve from Medtronic, was tested. Worthy of noting that the phase-averaged flow analysis revealed a jet of moderate velocity with an elliptical shape, the position of which varied in relation to the aorta wall during systole. This observation is congruent with the moving jet of moderate to high velocities noted for the VLth30 valvular case characterised by a varying eccentricity distance and angle of the jet over systole.

3.2. Vortical structures

In Fig. 5, the image sequence of the intricate coherent vortical structures downstream of the aortic stenosis and the two BioAVs is visualised using the λ_2-criterion [34]. In the stenotic case, we note a starting vortex ring hugging the shape of the stenotic orifice. The high difference in velocity between the accelerating flow (maximum velocity in the stenotic jet of 1.9 m/s) and the quiescent flow close to the wall of the aorta brings about zones of high shear at the interface propitious for the roll-up and shedding of eddies. This initial vortical structure is then shed and broken into smaller vortices that occupy the whole straight aorta volume under the push of a high velocity jet. From time $t = 0.09$ s onward, due to the impingement of the jet on the outer wall of the curved ascending aorta, as presented in Corso et al. [14], a secondary retrograde helical mean flow motion with smaller velocities is created in the curved portion of the aorta and pushes the majority of the vortical structures towards the outer aortic wall accentuating the asymmetry in the spatial distribution of the vortical structures. The high velocity jet is thus confined in the outer wall region throughout the whole systole. At the interface between the high-velocity jet and the low-flow regions near the inner wall, the entrainment of fluid with low momentum at the shear layers leads to intermittent increases in the number of small-scale densely distributed vortices at times $t = 0.12$, 0.18, 0.21 and 0.27 s. This intermittent surge in vortex break-up is mainly located close to the outer wall. The times at which it occurs coincide with the time instants at which slightly decelerating inflow velocities upstream of the stenosis are imposed (see Fig. S11 in the SI). With regard to the VLth30 BioAV case, initial coherent vortices

are found along the free edge of the leaflets (t=0.03 s). These vortices quickly dissipate due to leaflet motion. However, starting at $t = 0.03$ s, new vortical structures resembling hairpin vortices (as seen in the inset of Fig. 5 at $t = 0.06$ s) form in the gaps between the leaflet commissures and above the ring posts. In fact, the movement of the ring posts, resulting from the unstable motion of the leaflets, initiates the generation of hairpin-like vortical structures, particularly when the gaps widen. At $t = 0.09$ s, we note large vortical structures stretched in the axial direction issuing from the moving leaflet free edges. These are even more noticeable in the video in the SI between times $t = 0.09$ and $t = 0.12$ s. Between $t = 0.12$ and 0.21 s (after the inflow conditions reach the peak flow), due to flow deceleration, the coherent vortical structures are broken down into small vortices uniformly distributed over the whole straight ascending aorta as a consequence of the moving leaflets and valve orifice promoting higher mixing and vortex merging further downstream. Besides, large coherent eddies are displayed close the leaflet free edges and in the low velocity regions whereas stretched and smaller eddies are found in the shear layers, i.e. at the interface between the high velocity jet and the surrounding quiescent fluid close to the aorta wall. Between $t = 0.24$ and $t = 0.3$ s, the breakdown of the vortex is diminished as compared to previous times due to a reduction in jet velocity. However, the presence of large-scale vortical structures, induced by the motion of the leaflets, is still observable. In the Ulth0 BioAV case, a pattern reminiscent of the VLth30 case emerges, characterised by an initial vortex ring at the leaflets' free edge. It is interesting to note that up until $t = 0.06$ s, the jet of fluid maintains a circular shape, aligning with the contours of the orifice. Due to the flow acceleration, beyond $t = 0.06$ s, the shape of the jet becomes triangular. The initial vortex ring sheds and fades after $t = 0.03$ s owing to the formation of new eddies at the ring posts. In fact, akin to the VLth30 BioAV case, hairpin-shaped vortices are found at the ring post at $t = 0.06$ s due to the commissural gap between the leaflets (see inset at $t = 0.06$ s in Fig. 5). Unlike the other BioAV case though, between $t = 0.12$ and $t = 0.21$ s, these hairpin-shaped vortices demonstrate a tendency to elongate axially before being broken down into smaller vortices further downstream. This change in vortex shape is instigated by heightened shear between the triangular jet of elevated velocities (peaking at 1.8 m/s) and the surrounding zones of low velocity. Consequently, the presence of the three ring posts under stable leaflet motion condition, as the one observed in the Ulth0 BioAV case (cf. Fig. 3 (c)), has a pivotal influence on the distribution and size of the vortices downstream of the valve. From $t = 0.21$ s onward, the number of coherent vortical structures dwindles as a result of the flow deceleration as illustrated in Fig. S11 of the SI.

3.3. Momentum balance

To compare the results downstream of the three valvular configurations examined in this study with the findings of Chen and Luo [38] and Becsek et al. [7] and to evaluate the flow resistance resulting from the presence of prosthetic or stenotic valves, we compute each term of the flow momentum balance in the streamwise direction within a control volume V_{con}. The latter corresponds to the fluid present in both the ascending aorta and the sinus. The examined quantities, derived from the momentum balance equation and non-dimensionalised using the maximum pressure flux difference over systole, are listed below and presented in Table 1:

- the pressure term ΔPA averaged over systole;
- the acceleration term $\dot{p} = \frac{\partial}{\partial t} \iiint_{V_{con}} \rho u_z \, dV$ averaged over the systole with V_{con}, the control volume;
- the mean and maximal drag coefficient $C_D = \left(2F_{\text{leaflets}}\right) / \left(\iint_{in} \rho u_z^2 dA\right)$ with F_{leaflets}, the total hydrodynamic force acting on the leaflet surfaces and the denominator being the inlet momentum flux;

Table 1
Table of the non-dimensional quantities based on the terms of the momentum conservation along the streamwise direction for the three valvular cases presented in this work and for the cases presented in Chen and Luo [38] and Becsek et al. [7].

	$\overline{\Delta P A}$	$\overline{\dot{p}}$	$\overline{C_D}$	max C_D	$\overline{h_{F_{\text{leaflets}}}}/\varnothing$
1. Stenotic — Corso et al. [2]	0.746	0.037	1.42	3.36 at t=0.083 s	2
2. BioAV — VLth30	0.432	0.14	0.175	0.24 at t=0.108 s	0.5
3. BioAV — Ulth0	0.459	0.072	0.103	0.14 at t=0.154 s	0.33
4. BioAV — similar case as that presented in Becsek et al. [7]	0.387	0.081	0.502	0.94 at t=0.122 s	1.12
5. Flexible AV — Chen and Luo [38]	0.477	0.16	0.47	1.04 at t=0.18 s	2.23

• the mean equivalent length of accelerated fluid column $h_{F_{\text{leaflets}}} = \left(LF_{\text{leaflets}}\right)/\dot{p}$ made dimensionless by dividing it by the reference diameters $\varnothing_{\text{sten}} = 0.011$ m and $\varnothing_{\text{BioAV}} = 0.018$ m. L is the length (in the Z-direction) of the control volume.

Table 1 shows that the time-averaged dimensionless pressure flux difference is of a comparable magnitude for the bioprosthetic cases (lines 2, 3, 4 in Table 1) and the flexible aortic valve case (line 5 in Table 1) but it is 67% higher in the stenotic case. This larger value can be attributed to stenosis, which introduces larger pressure loss as well as to the curved aorta geometry in the stenotic case, which modifies the position where pressure recovery arises [39]. In addition, in the stenotic case, the time-averaged acceleration term is two to four times as small as that calculated in the four prosthetic aortic valve cases. With regard to the drag coefficient C_D, the mean and maximal values for the cases presented in Becsek et al. (line 4 in Table 1) and Chen and Luo (line 5 in Table 1) are in good agreement. This can be attributed to the observed strong periodic flutter of the leaflets [7,38]. This type of flutter motion leads to the generation of a sequence of vortex rings, whose shapes vary over time [38]. For the other two BioAV cases studied in this work (lines 2 and 3), the drag coefficient (C_D) values are one-fourth to one-fifth of those calculated from the data presented in [7,38]. The VLth30 case presents higher C_D value compared to the Ulth0 case as a consequence of the non-axisymmetric but moderate flutter motion (see Fig. S1 in the supplementary information). This underscores the influence of leaflet geometry on the resistive forces introduced by the aortic valve prosthesis and its correlation with the type of flutter motions exhibited by the leaflets. In relation to the equivalent length of the fluid column $\overline{h_{F_{\text{leaflets}}}}$ decelerated due to the reaction forces at the leaflet surfaces, the stenotic case displays the highest value. However, for the valvular cases demonstrating periodic flutter of the leaflets with substantial displacement magnitudes (lines 4 and 5 in Table 1 corresponding to the flexible valve scenarios presented by Chen and Luo [38] and by Becsek et al. [7]), the decelerated fluid column due to the presence of the valve falls within a similar range as that observed in the case of aortic stenosis . The newly designed BioAV cases, namely VLth30 and Ulth0, exhibit values for $\overline{h_{F_{\text{leaflets}}}}$ that are 4 and 6 times smaller than the value calculated in the stenotic case, respectively.

### 3.4. Vorticity transport and vortex stretching

Fig. 6 allows for the comparison of vorticity amongst three different aortic valve types: stenotic, bioprosthetic and native. The spatially and temporally averaged L1-norm of the vorticity vector downstream of these three types at peak systole is presented. To complement the numerical data produced for the present study, data from *in vitro* tomo-PIV measurements [33] and from four-dimensional magnetic resonance imaging [13] are utilised. It is noteworthy that the reduction in vorticity compared to the stenotic case is rather marginal, i.e., below 10%, for the BioAV valve design proposed in Becsek et al. [7]. As highlighted in the previous subsection by calculating each term of the one-dimensional momentum balance equation, detrimental effects due to periodic leaflet motions with high displacement magnitudes are not only relevant for structural degeneration [8] but also for haemodynamic performance. In the VLth30 BioAV case, the reduction is 27%, which is in a similar range as the vorticity reduction in relation

to the stenotic case obtained from the *in vitro* experiments on the *Edwards Intuity Elite* BioAV. The reduction for the Ulth0 BioAV design is 50%, suggesting that the latter valve is haemodynamically more performant than the native BAV and performs more closely to how a native TAV performs. As expected, the vorticity reduction is the highest (65%) for native tricuspid aortic valves as derived from the flow evaluated *in vivo* on healthy patients [13]. The evaluation of spatially and temporally averaged L1-norm of the vorticity vector is informative for haemodynamic performance evaluation as it accounts for the suppression of turbulence-related vortical structures.

In the following paragraph, we analyse the vortex straining term S_ω and the advection due to the flow velocity A_ω of the vorticity transport equation (cf. Eq. (2)). This transport equation is central for the characterisation of the evolution and distribution of vortices, especially pertaining to their amplification or decay at the considered time instance.

In Fig. 7 (a), the evolution of the magnitude of the vortex straining tensor averaged over the VoI is presented. In the stenotic case, $\langle\|S_\omega\|\rangle$ generally decreases over systole with 5 peaks occurring at $t = 0.125$, 0.143, 0.193, 0.25 and 0.28 s. The peaks observed, ranging between 1.85×10^5 and $2.8 \times 10^5 \text{ s}^{-2}$, correspond to instances when a higher density of vortical structures were identified in Fig. 5. In the VLth30 case, between $t = 0.135$ s and 0.156 s, peak values of $1.76 \times 10^5 \text{ s}^{-2}$ are exhibited following the trend of the inflow rate time series consisting of an acceleration until $t = 0.1$ s and a two-third less deceleration until $t = 0.21$ s (cf. Fig. S11 in the SI). In the Ulth0 case, a peak value of $1.38 \times 10^5 \text{ s}^{-2}$ is observed at $t = 0.186$ s. The rate of change over time for the vortex straining magnitude in this case is nearly identical. Finally, the time-averaged $\langle\|S_\omega\|\rangle$ presented in the table of Fig. 7 (d) is twice as large for the stenosed aorta case compared to the values calculated in the two BioAV cases.

The time series of the ensemble-averaged projected vortex stretching $\langle\Pi^{S_\omega}\rangle$ as defined in Eq. (3) is shown in Fig. 5 (b). It is noteworthy that the majority of values are highly positive in the case of calcific stenosis, especially up to $t = 0.23$ s. Positive projected vortex stretching, averaged over the VoI and reaching a maximum value of $1.33 \times 10^4 \text{ s}^{-2}$ in the stenotic case, indicates an alignment between the vorticity vector and the principal directions of the rate-of-strain tensor, multiplied by the eigenvalues of this tensor. It represents a phenomenon called vorticity amplification or intensification [40] characterised by the elongation of vortical structures and an increase in the rotational motions in the flow. In Fig. S8 of the SI, we observe that the stenotic orifice in the proximal plane is delineated by high and locally concentrated negative values of the Π^{S_ω} field, especially from $t = 0.18$ s onward. The presence of this ridge of projected vortex stretching draws parallel with LCS, which were highlighted in Shadden et al. [12] through high values of backward time FTLE fields. In the VLth30 bioprosthetic case, positive levels of $\langle\Pi^{S_\omega}\rangle$ are found between $t = 0.11$ and 0.156 s and between $t = 0.19$ and 0.22 s with a maximum of $3.5 \times 10^3 \text{ s}^{-2}$ and on average over systole, the projected vortex stretching is positive (see Fig. 7 (d)). In contrast, the levels of $\langle\Pi^{S_\omega}\rangle$ for the Ulth0 case are mainly negative. This results, as shown in the table of Fig. 7 (d), in a negative time-averaged value, which is 4.7 times smaller in magnitude than that for the stenotic case and 4.4 times larger than the one obtained for the VLth30 BioAV case. It is worth noting that negative projected vortex stretching is associated with an anti-parallel alignment of the vorticity
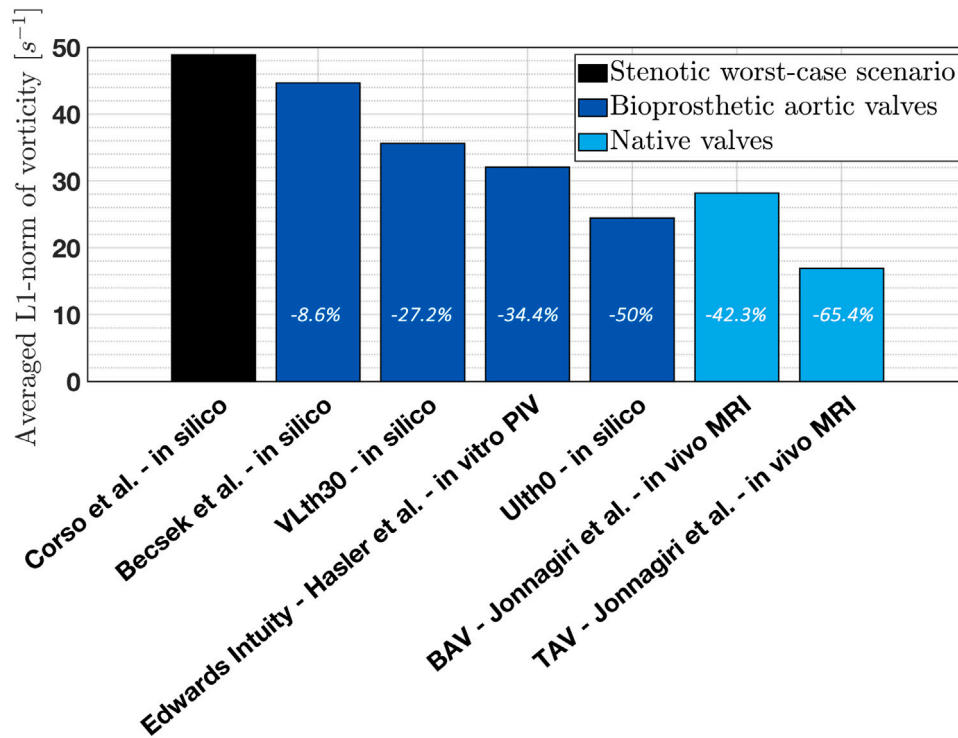
Fig. 6. Bar chart of the L1-norm of the vorticity vector averaged over two proximal planes at peak systole downstream of different valvular configurations. Three categories of aortic valves are displayed: (i) aortic valve stenosis [1,2,14], (ii) bovine pericardial biological valves (new designs proposed in the present study referred to as Ulth0, VLth30, the design presented in [7] and the *Edwards Intuity Elite* [33]), (iii) native bicuspid aortic valve (BAV) and tricuspid native valve (TAV). The flow data used to compute the vorticity vector are obtained from three different modalities: *in silico* simulations as presented in the present study and in [2,7,14], *in vitro* tomographic particle image velocimetry [33] and *in vivo* time-resolved and three-dimensional flow magnetic resonance imaging [13].

vector and the strain rate, resulting in a decrease in overall vorticity acceleration, a phenomenon known as vorticity attenuation [40]. This attenuation is linked to the favourable reorganisation of the flow and the suppression of flow disturbances. In Fig. S8 of the SI, for the Ulth0 case, similarly to the stenotic case, the valvular orifice projects onto a proximal plane as material lines forming a triangle with high Π^{S_ω} values albeit in the Ulth0 BioAV case, the values are mainly positive throughout systole. The triangular shape of the jet was also outlined for the simulated valvular case in [12] and revealed by attracting LCS.

Fig. 7 (c) shows the time evolution of the ensemble-averaged projected vorticity advection $\langle \Pi^{A_\omega} \rangle$, which represents the intensity whereby vorticity is transported by the velocity field. In fact, a positive (negative) value indicates that the velocity vector is parallel (anti-parallel) to the principal directions of the vorticity gradient tensor and the magnitude is the result of the multiplication of the latter by the eigenvalues of the vorticity gradient tensor. In other words, positive ensemble-averaged projected vorticity advection values indicate that spatial variations in the vorticity field primarily occur along the flow direction, while negative values suggest that the advection of the vorticity field predominantly opposes the flow direction. For the aortic valve stenosis case, we observe that $\langle \Pi^{A_\omega} \rangle$ levels are, for the most part of systole, positive leading to a large time-averaged value of 9,157 s^{-2} as shown in the table of Fig. 7 (d). We also note that this time-averaged $\langle \Pi^{A_\omega} \rangle$ is 3.65 times as large as the time-averaged $\langle \Pi^{S_\omega} \rangle$ and of the same sign. Concerning the VLth30 bioprosthetic valve case, $\langle \Pi^{A_\omega} \rangle$ alternates between positive and negative values over systole resulting in a negative time-averaged value. The times at which these negative and positive peaks occur are coincident with the times of the peaks observed in Fig. 3 (c) for the area at the vena contracta. Thereby, the asymmetric leaflet motion does play an important role in the transport of vortices in the region downstream of the valve albeit not necessarily by promoting the advection of the vorticity field in the flow direction but in an opposite direction as well. Finally, the magnitude of time-averaged $\langle \Pi^{A_\omega} \rangle$ is in this case 2.8 times as large as the time-averaged

$\langle \Pi^{S_\omega} \rangle$. For the Ulth0 case, the most favourable conditions are met to fulfil vorticity weakening in the bulk of the flow downstream of the valve with a positive time-averaged $\langle \Pi^{A_\omega} \rangle$, whose magnitude is 26% less than the magnitude of time-averaged $\langle \Pi^{S_\omega} \rangle$. As previously stated, the latter is negative highlighting a more pronounced vorticity attenuation over the VoI.

4. Conclusions

The findings for each valvular case regarding this first part of the study can be summarised as follows:

- Stenotic case: In the stenotic case, where the orifice geometry is assumed to be immobile due to heavily calcified leaflets, jet eccentricity remains relatively constant throughout the systolic phase. This stable jet position is accompanied by elevated velocity magnitudes and vortex straining between specific commissures. The vortical structures downstream of the aortic stenosis feature an initial vortex ring hugging the orifice shape, which subsequently breaks into smaller vortices under the influence of high shear zones. A secondary retrograde helical flow motion develops close to the inner aortic wall in consequence of the impingement of the jet on the outer wall of the curved ascending aorta, confining the high-velocity jet to the outer wall region. Intermittent vortex break-up occurs at the interface between the high-velocity jet and low-flow regions near the inner wall, coinciding with time instances of slightly decelerating inflow velocities. The equivalent length of the decelerated fluid column is highest in the stenotic case, reflecting greater resistance to flow. The time-averaged magnitude of the vortex straining tensor is generally decreasing over systole, with several peaks indicating higher density of vortical structures. Positive projected vortex stretching suggests vorticity amplification and the time-averaged ensemble-averaged projected
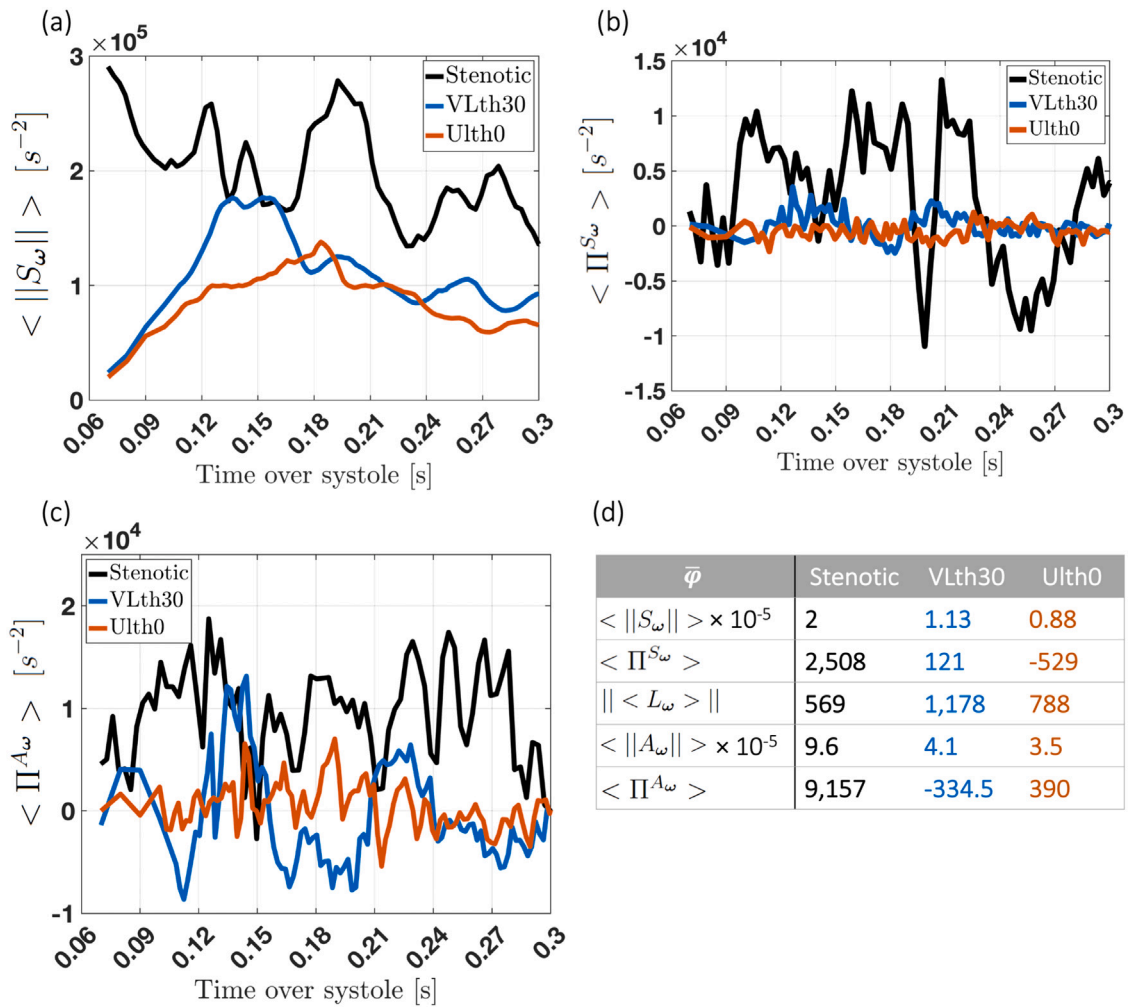
Fig. 7. Quantities based on the terms of the vorticity dynamics equation for the three valvular cases. (a) Time evolution of the spatially averaged vortex straining magnitude. (b) Time series of the projected vortex stretching averaged over the VoI. (c) Time series of the projected vortex advection averaged over the VoI. (d) Table with the spatially and temporally averaged quantities of the vorticity transport equation.

vorticity advection is positive, indicating the transport of vortices primarily along the flow direction and with an intensity larger than the intensity of their attenuation.

- VLth30 BioAV case: In contrast to the stenotic case, the eccentricity distance and angle vary throughout the systolic phase in this case due to the asymmetric movement of the three leaflets. Consequently, the maximum velocity in the jet decreases compared to the stenotic case. The velocity distribution surrounding the jet is poorly organised, with larger velocity values attributed to leaflet motion pushing blood towards the wall and promoting mixing of high and low-velocity zones. Coherent vortices initially form along the leaflets' free edge and along the valve ring, with hairpin-like vortical structures generated by leaflet motion and ring post movement. Large vortical structures stretched in the axial direction emerge from the moving leaflet free edges. Subsequent flow deceleration leads to the breakdown of coherent vortical structures into smaller vortices, promoting higher mixing and vortex merging further downstream. Drag coefficient value is higher compared to the Ulth0 case due to non-axisymmetric and moderate flutter motion. The equivalent length of the decelerated fluid column is significantly smaller compared to the stenotic case but larger than the Ulth0 BioAV case, indicating intermediate resistance to flow. The reduction in vorticity compared to the aortic stenosis case is 27% and similar to the reduction obtained from

in vitro experiments on the *Edwards Intuity Elite* BioAV. Positive temporally and spatially averaged projected vortex stretching indicates vorticity amplification, albeit with an intensity one order of magnitude lower than that of the stenotic case. The ensemble-averaged projected vorticity advection alternates between positive and negative values over systole, indicating advection of vortices in both streamwise and counter-streamwise directions as a result of the leaflet motions.

- Ulth0 BioAV case: In this scenario, where leaflets are nearly immobile at peak systole, the eccentricity distance is negligible, resulting in a well-defined triangular-shaped jet. However, instabilities are observed in the shear layer between the high-velocity jet and the surrounding quiescent region at certain time instants. These instabilities, known as Kelvin–Helmholtz instability (KHI), manifest as wavy irregularities in the velocity distribution at the borders of the triangular jet. Similar to the VLth30 case, an initial vortex ring forms at the leaflets' free edge. Hairpin-shaped vortices are generated at the ring posts, which elongate axially before breaking down into smaller vortices. Coherent vortical structures diminish in number due to flow deceleration over time. Drag coefficient values are lower compared to the VLth30 case due to stable leaflet motion. The equivalent length of the decelerated fluid column is the smallest among all cases, indicating the least resistance to flow. The reduction

in vorticity compared to the stenotic case is 50%, suggesting better haemodynamic performance compared to native bicuspid valves and akin to native tricuspid valves. Negative temporally and spatially averaged projected vortex stretching Π^{S_ω} indicates vorticity attenuation. The time-averaged and ensemble-averaged projected vorticity advection Π^{A_ω} is positive but with an absolute value smaller than the value of time-averaged $\langle \Pi^{S_\omega} \rangle$, indicating beneficial reorganisation of blood dynamics, which suppresses disturbances.

The insights gained from this study significantly contribute to the broader understanding of blood and valve dynamics associated with stenotic and prosthetic aortic valves. The study introduces novel quantities to extract and analyses to perform *in silico*, *in vitro* or *in vivo* in order to thoroughly assess the performance of valve prostheses. This is achieved by comparing the field quantities between stenotic, bioprosthetic and healthy valvular scenarios. Furthermore, the study demonstrates in detail how dedicated geometrical features of valve leaflets influence the structural behaviour and downstream haemodynamics of BioAVs. The Ulth0 valve design is proposed as the enhanced standard for bovine pericardial BioAVs since it promotes a more organised and physiological flow, which, in turn, results in reduced pressure loss and decreased haemodynamic forces acting on blood cells and the aortic wall. The limitations of this first part of the study include the absence of the sinus portion for the stenosed aorta case. Indeed, the study focuses on the analysis of jet flow configuration and subsequent vortical structures arising from the interaction between the jet and the surrounding low-flow region, which, for the stenotic case, due to the narrowed stenotic orifice geometry, is concentrated in the aorta. Besides, the acquisition parameters for the high-resolution MRI scan used to obtain the geometry of the severely stenosed aorta of a patient are no longer available as the scan was conducted about 15 years ago for previous studies (e.g. [1,2,14]). Only the systolic phase is simulated, as blood flow disturbances are mainly generated during this phase of the cardiac cycle and unstable leaflet motions principally occur when the valve is open. Another limitation is the straight and shorter aorta geometry for the BioAV cases. This is deemed acceptable because (i) it enables the relative reduction in the computational costs associated with resolving high-fidelity FSI problems and (ii) the focus of the present study is on the interplay between leaflet geometry, flow structures, vorticity and leaflet dynamics.

The two-part computational study paves the way for the development, through dedicated aortic flow data analyses, of innovative and patient-customised valve designs that can optimise systolic flow patterns and minimise detrimental effects associated with aortic valve replacement.

CRediT authorship contribution statement

Pascal Corso: Writing – review & editing, Writing – original draft, Visualization, Validation, Software, Resources, Project administration, Methodology, Investigation, Formal analysis, Data curation, Conceptualization. **Dominik Obrist:** Resources, Funding acquisition.

Declaration of competing interest

The authors declare that they have no known competing financial interests or personal relationships that could have appeared to influence the work reported in this paper.

Data availability

All data and materials needed to evaluate the conclusions of this paper are present in the main text or supplementary materials. Processable data files can be obtained from the first author.

Appendix A. Supplementary data

Supplementary material related to this article can be found online at https://doi.org/10.1016/j.compbiomed.2024.108526.

References

[1] P. Corso, U. Gülan, N. Cohrs, et al., Comprehensive in vitro study of the flow past two transcatheter aortic valves: Comparison with a severe stenotic case, Ann. Biomed. Eng. 47 (11) (2019) 2241–2257.

[2] P. Corso, G. Giannakopoulos, U. Gulan, et al., A novel estimation approach of pressure gradient and haemodynamic stresses as indicators of pathological aortic flow using subvoxel modelling, IEEE Trans. Biomed. Eng. 68 (3) (2021) 980–991.

[3] A.J. Yoganathan, S. He, S.C. Jones, Fluid mechanics of heart valves, Annu. Rev. Biomed. Eng. 6 (2004) 331–362.

[4] S.H. Pujari, P. Agasthi, Aortic stenosis, in: StatPearls [Internet], StatPearls Publishing, Treasure Island (FL), 2023, [Online]. Available https://www.ncbi.nlm.nih.gov/books/NBK557628/.

[5] V. Nguyen, M. Michel, H. Eltchaninoff, et al., Implementation of transcatheter aortic valve replacement in France, J. Am. Coll. Cardiol. 71 (15) (2018).

[6] S. Bailoor, J.-H. Seo, L. Dasi, et al., A computational study of the hemodynamics of bioprosthetic aortic valves with reduced leaflet motion, J. Biomech. 120 (2021).

[7] B. Becsek, L. Pietrasanta, D. Obrist, Turbulent systolic flow downstream of a bioprosthetic aortic valve: Velocity spectra, wall shear stresses, and turbulent dissipation rates, Front. Physiol. 11 (2020) 539–575.

[8] E.L. Johnson, M.C.H. Wua, F. Xu, et al., Thinner biological tissues induce leaflet flutter in aortic heart valve replacements, Proc. Nat. Acad. Sci. USA 117 (32) (2020) 19007–19016.

[9] A. Morany, K. Lavon, R.G. Bardon, B. Kovarovic, A. Hamdan, D. Bluestein, R. Haj-Ali, Fluid–structure interaction modeling of compliant aortic valves using the lattice Boltzmann CFD and FEM methods, Biomech. Model. Mechanobiol. 22 (2023) 837–850.

[10] G. Marom, M. Peleg, R. Halevi, et al., Fluid–structure interaction model of aortic valve with porcine-specific collagen fiber alignment in the cusps, J. Biomech. Eng. 135 (10) (2013).

[11] A.B. Olcay, A. Amindari, K. Kirkkopru, H.C. Yalcin, Characterization of disturbed hemodynamics due to stenosed aortic jets with a Lagrangian coherent structures technique, J. Appl. Fluid Mech. 11 (2) (2018) 375–384.

[12] S.C. Shadden, M. Astorino, J.-F. Gerbeau, Computational analysis of an aortic valve jet with Lagrangian coherent structures, Chaos 20 (2010) 1–11.

[13] R. Jonnagiri, E. Sundström, E. Gutmark, S. Anderson, A.S. Pednekar, M.D. Taylor, J.T. Tretter, I. Gutmark-Little, Influence of aortic valve morphology on vortical structures and wall shear stress, Med. Biol. Eng. Comput. 61 (2023) 1489–1506.

[14] P. Corso, J. Walheim, H. Dillinger, et al., Toward an accurate estimation of wall shear stress from 4D flow magnetic resonance downstream of a severe stenosis, Magn. Res. Med. 86 (3) (2021) 1531–1543.

[15] F.B. Coulter, M. Schaffner, J.A. Faber, A. Rafsanjani, R. Smith, H. Appa, P. Zilla, D. Bezuidenhout, A.R. Studart, Bioinspired heart valve prosthesis made by silicone additive manufacturing, Matter 1 (2019) 266–279.

[16] Y. Izawa, S. Mori, J.T. Tretter, J.A. Quintessenza, et al., Normative aortic valvar measurements in adults using cardiac computed tomography - A potential guide to further sophisticate aortic valve-sparing surgery, Circ. J. 85 (7) (2021) 1059–1067.

[17] NEK5000 v19.0, Argonne national laboratory, Illinois, 2020, [Online]. Available: https://nek5000.mcs.anl.gov.

[18] M.O. Deville, P.F. Fischer, E.H. Mund, Unsteady Stokes and Navier–Stokes equations, in: High-Order Methods for Incompressible Fluid Flow, in: Cambridge Monographs on Applied and Computational Mathematics, Cambridge University Press, 2002, pp. 291–332.

[19] P. Corso, D. Obrist, On the role of aortic valve architecture for physiological hemodynamics and valve replacement. Part II: spectral analysis and anisotropy, Comput. Biol. Med. (2023).

[20] Ch.S. Peskin, The immersed boundary method, Acta Numer. 11 (2002) 479–517.

[21] M.G. Ch. Nestola, B. Becsek, H. Zolfaghari, et al., An immersed boundary method for fluid–structure interaction based on variational transfer, J. Comput. Phys. 398 (2019).

[22] E. Tsolaki, P. Corso, R. Zboray, J. Avaro, et al., Multiscale multimodal characterization and simulation of structural alterations in failed bioprosthetic heart valves, Acta Biomater. 169 (10) (2023) 138–154.

[23] R. Henniger, D. Obrist, L. Kleiser, High-order accurate solution of the incompressible Navier–Stokes equations on massively parallel computers, J. Comput. Phys. 229 (10) (2010) 3543–3572.

[24] C.J. Permann, D.R. Gaston, D. Andrs, R.W. Carlsen, F. Kong, A.D. Lindsay, et al., MOOSE: Enabling massively parallel multiphysics simulation, SoftwareX 11 (2020).

[25] S. Balay, S. Abhyankar, M.F. Adams, S. Benson, J. Brown, et al., PETSc web page, 2023, [Online]. Available: https://petsc.org/.

[26] R. Krause, P. Zulian, A parallel approach to the variational transfer of discrete fields between arbitrarily distributed unstructured finite element meshes, SIAM J. Sci. Comput. 38 (3) (2016).

[27] F. Auricchio, M. Conti, A. Ferrara, S. Morganti, A. Reali, Patient-specific simulation of a stentless aortic valve implant: the impact of fibres on leaflet performance, Comput. Methods Biomech. Biomed. Eng. 17 (3) (2014) 277–285.

[28] G.A. Holzapfel, Th.C. Gasser, R.W. Ogden, A new constitutive framework for arterial wall mechanics and a comparative study of material models, J. Elasticity 61 (1) (2000) 1–48.

[29] A.D. Caballero, S. Laín, A review on computational fluid dynamics modelling in human thoracic aorta, Cardiovasc. Eng. Technol. 4 (2) (2013) 103–130.

[30] D.J. Bodony, Analysis of sponge zones for computational fluid mechanics, J. Comput. Phys. 212 (2006) 681–702.

[31] C. Canuto, M.Y. Hussaini, A. Quarteroni, T.A. Zang, Single-domain methods for incompressible flows, in: Spectral Methods: Evolution to Complex Geometries and Applications to Fluid Dynamics, Springer, Berlin Heidelberg, 2007, pp. 159–161.

[32] P. Petitjeans, Stretching of a vortical structure: filaments of vorticity, Europhys. News 34 (1) (2003) 20–23.

[33] D. Hasler, D. Obrist, Three-dimensional flow structures past a bio-prosthetic valve in an in-vitro model of the aortic root, PLOS ONE 13 (3) (2018).

[34] J. Jeong, F. Hussain, On the identification of a vortex, J. Fluid Mech. 285 (1995) 69–94.

[35] A. Sciacchitano, B. Wieneke, PIV uncertainty propagation, Meas. Sci. Technol. 27 (2016) 1–16.

[36] P. Corso, F. B.Coulter, M.G. Ch. Nestola, et al., Study of the flutter kinematics and blood flow motion for bioprosthetic aortic valves with different designs, in: Heart Valve Society's Annual Meeting, 2022, unpublished.

[37] S. Friedlander, A. Lipton-Lifschitz, Localized instabilities in fluids, in: Handbook of Mathematical Fluid Dynamics, 2003, pp. 289–354.

[38] Y. Chen, H. Luo, A computational study of the three-dimensional fluid–structure interaction of aortic valve, J. Fluids Struct. 80 (2018) 332–349.

[39] B. Vogl, R. Gadhave, Z. Wang, et al., Effect of aortic curvature on bioprosthetic aortic valve performance, J. Biomech. 146 (1) (2023).

[40] M.H. Williams, Vorticity amplification and annihilation in a potential vortex, Phys. Fluids 4 (1992) 1467–1471.